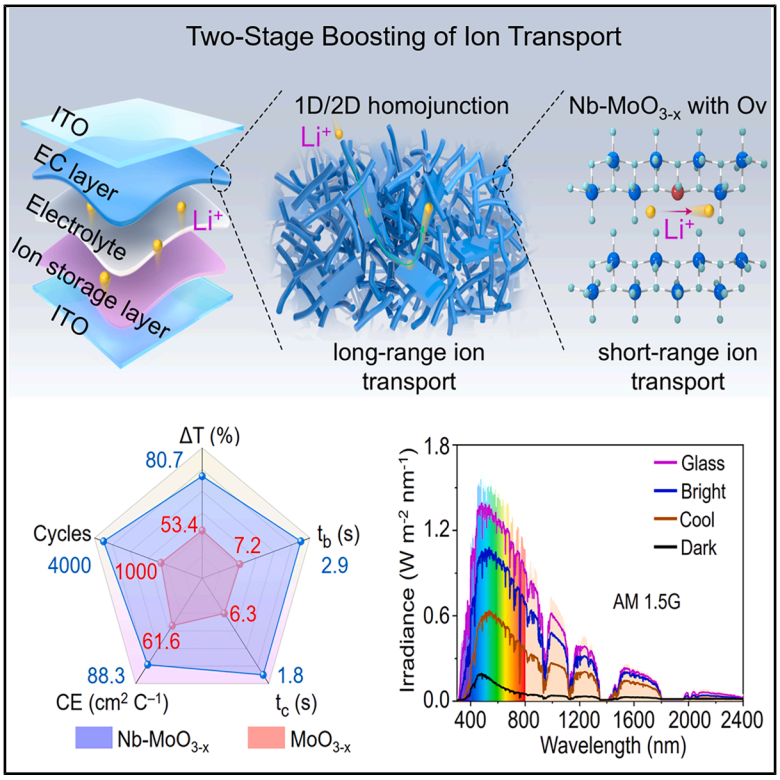
Matter & Light

Article

Two-stage boosting of ion transport in electrochromic Nb–MoO_{3-x} homojunction

Graphical abstract



Highlights

- A two-stage strategy synergistically boosts short-range and long-range ion transport
- The homojunction exhibits large transmittance modulation and ultrafast switching
- A large-area device with low voltage and outstanding heat insulation was prepared

Authors

Haolin Yu, Kai Jing, Huajing Fang, Qing Zhao, Yuanbin Qin, Yang Chai

Correspondence

fanghj@xjtu.edu.cn (H.F.), ychai@polyu.edu.hk (Y.C.)

In brief

This work provides an easy yet effective strategy to realize a metal oxide homojunction. The Nb-MoO_{3-x} homojunction exhibits outstanding electrochromic performance including large transmittance modulation (80.7%), fast switching speed (t_b = 2.9 s, t_c = 1.8 s), and excellent long-term stability (up to 4,000 cycles). The synergistic effect of element doping and morphology modulation to improve long-range and short-range ion transport can also be referenced in other electrochemical fields.

Improvement
Enhanced performance with innovative design or material control

Yu et al., 2026, Matter & Light *1*, 100137
October 8, 2026 © 2026 The Author(s). Published by Elsevier Inc.
https://doi.org/10.1016/j.matlit.2026.100137

CellPress

Matter & Light

CellPress
OPEN ACCESS

Article

Two-stage boosting of ion transport in electrochromic Nb–MoO_{3-x} homojunction

Haolin Yu,[1] Kai Jing,[1] Huajing Fang,[1,3,*] Qing Zhao,[1] Yuanbin Qin,[1] and Yang Chai[2,*]
[1]Center for Advancing Materials Performance from the Nanoscale (CAMP-Nano), State Key Laboratory for Mechanical Behavior of Materials, Xi'an Jiaotong University, Xi'an 710049, China
[2]Department of Applied Physics, The Hong Kong Polytechnic University, Hong Kong 999077, China
[3]Lead contact
*Correspondence: fanghj@xjtu.edu.cn (H.F.), ychai@polyu.edu.hk (Y.C.)
https://doi.org/10.1016/j.matlit.2026.100137

PROGRESS AND POTENTIAL Boosting the ion transport in metal oxides is crucial but challenging due to the complex process across spatial scales. According to the characteristic of ion transport, it can be classified into two categories: short-range ion transport usually refers to the movement within the lattice size, and long-range ion transport spanning the full thickness of the functional layer. Thus, this work presents a two-stage optimization based on the Nb-doped MoO_{3-x} homojunctions to simultaneously address the inherent issues of poor long-range and short-range ion transport. The Nb doping in MoO_{3-x} increases the ion diffusion coefficient by an order of magnitude as the short-range Li^+ diffusion barrier is reduced. Meanwhile, the homojunctions consist of 1D nanowires and 2D nanosheets that establish a robust framework for enhancing long-range ion transport and suppressing the structural collapse. This research provides a promising solution for the optimization of ion transport in electrochromic and other electrochemical fields.

SUMMARY

Smart windows based on metal oxides enable dynamic solar radiation regulation, yet the practical application is hindered by the poor electrochromic performance caused by sluggish kinetics. Boosting the ion transport in metal oxides is crucial but challenging due to the complex process across spatial scales. Herein, we propose a two-stage optimization strategy based on the Nb–MoO_{3-x} homojunction, which synergistically boosted the short-range and long-range ion transport. The optimized electrochromic device based on the Nb–MoO_{3-x} homojunction exhibits large transmittance modulation (ΔT = 80.7%), ultrafast switching speed (t_b = 2.9 s, t_c = 1.8 s), and superior cycling stability (91.9% retention after 4,000 cycles), resulting in an unprecedented level of comprehensive performance in molybdenum oxide. Furthermore, we demonstrate a large-area electrochromic device with excellent heat management capability and a low driving voltage of 1.5 V. This work proposes a distinctive method for building metal oxide homojunctions and provides a two-stage optimization strategy for future electrochromic energy-saving applications.

INTRODUCTION

Electrochromic smart windows have demonstrated considerable potential in the low-carbon domains of energy-efficient buildings and transportation, owing to the integration of dynamic spectral control and thermal management functions.[1–4] Inorganic electrochromic metal oxides demonstrate the capacity for extensive spectral modulation, effectively regulating the spectrum from visible light to the near-infrared band.[5–7] Among them, molybdenum oxide (MoO_3) is a highly promising candidate material with advantages such as environmental compatibility, abundant resources, as well as the eye-friendly colored state.[8,9] The electrochromic behavior of metal oxides such as MoO_3 depends on reversible electrochemical reactions. Taking cathodic-type electrochromic metal oxides as an example, the coloring process is caused by the insertion of Li^+ ions or other cations, while the bleaching process is caused by the extraction of cations.[10] Therefore, ion transport plays a crucial role in the spectral regulation of electrochromic metal oxides. Unfortunately, most intrinsic metal oxides are wide-band-gap semiconductors with inferior conductivity and poor electrochemical kinetics related to ion transport efficiency. The low ion diffusion coefficient fundamentally limits the coloring and bleaching speed of electrochromic metal oxides. If certain lattice sites cannot be inserted with ions within a given time due to dynamic limitations (slow diffusion), the optical modulation (ΔT, a key electrochromic

This is an open access article under the CC BY license (http://creativecommons.org/licenses/by/4.0/).

parameter) will be difficult to expand. Moreover, smooth ion transport is a prerequisite for devices to efficiently and reversibly switch between the colored and bleached states. Once ions are trapped, this can result in slow transport kinetics between ions or stronger electrostatic repulsion, thereby preventing subsequent ions from entering the reversible sites to achieve electrochromism.[11–13] Thus, improving ion transport is a necessary path to break through the bottleneck of comprehensive performance for electrochromic metal oxides.

Ion transport in the electrochromic device is a complex mass transfer process across multiple scales. According to the characteristic length dimensions of ion transport, it can be classified into two categories: short-range ion transport usually refers to the movement within the lattice size, and long-range ion transport with lengths across the functional layer. Current research efforts aim to improve the short-range or long-range ion transport of electrochromic materials, often as separate objectives. For the former, introducing point defects and lattice distortion inside metal oxides has been extensively explored.[14–17] For instance, Cao et al. reported the W^{6+} doping in the shear-phase Nb_2O_5 with oxygen vacancies and ion-lattice coupling strength, leading to ultrastable dual-band electrochromism.[18] Han et al. revealed that active Ni vacancies can provide ion storage sites and promote the transport of lithium ions by forming diffusion channels in electrochromic nickel oxide electrodes.[19] Li et al. reported that the orthorhombic oxygen-deficient tungsten oxide films possess advanced dual-band electrochromic performance, which is attributed to the introduction of oxygen vacancies that can facilitate the adsorption and diffusion of ions.[20] These methods make the diffusion of ions in the lattice easier but cannot improve the transport of ions across different particles, so the long-range ion transport inside the device is still limited. Recent advancements have demonstrated that the application of heterogeneous composite materials is able to solve the long-range ion transport problem to a certain extent.[21–24] For example, Celebi et al. engineered the composite of MXene ($Ti_3C_2T_x$) nanosheets and $W_{18}O_{49}$ nanowires with enhanced transport kinetics for flexible electrochromic devices.[25] Our group demonstrated the method of boosting the long-range ion transport of two-dimensional molybdenum oxide nanoflakes by compositing them with conductive PEDOT:PSS polymer.[26] However, the components used to improve long-range ion transport in electrochromic composites are usually light-absorbing materials, which sacrifice the transmittance of the device in the bleached state. Zheng et al. reported that AgNWs (Ag nanowires) were utilized as sacrificial reducing agents to introduce oxygen vacancies and promote the growth of the $WO_{3-x} \cdot 2H_2O$/AgNWs composite films, aiming to improve electrochromic performance.[27] Unfortunately, challenges remain with regard to the uniform distribution of heterogeneous materials and compatibility with the base material, thereby increasing processing complexity and cost. So far, the collaborative improvement of long-range and short-range ion transport inside the electrochromic metal oxides still needs to be explored.

As a promising approach to designing novel optoelectronic devices, the homojunction has attracted significant attention owing to its unique properties such as homogeneous components, perfect lattice matching, and efficient charge transfer at the interface.[28] In this work, we present a two-stage optimization based on the *in-situ*-formed Nb–doped MoO_{3-x} homojunctions to simultaneously address the inherent issues of poor long-range and short-range ion transport in molybdenum oxide. Experimental results together with theoretical calculations reveal that the Nb doping inside the MoO_{3-x} has the capacity to facilitate short-range ion transport and reduce the diffusion energy barrier of lithium ions. Moreover, the Nb–doped MoO_{3-x} homojunction exhibits the advantages of both nanowires and nanosheets. It can effectively improve the long-range ion transport efficiency of lithium ions between different interfaces and establish a robust structure to alleviate the volume expansion during ion insertion/extraction processes. The Nb–MoO_{3-x} homojunction exhibits excellent comprehensive electrochromic performance, including large transmittance modulation ($\Delta T = 80.7\%$), ultrafast switching speed ($t_b = 2.9$ s, $t_c = 1.8$ s), and excellent long-term stability (up to 4,000 cycles). This research not only paves the way for the construction of metal oxide homojunctions but also provides a promising solution for the optimization of ion transport in electrochromic and other related electrochemical fields.

RESULTS

Figure 1A illustrates the two-stage optimization of the Nb–MoO_{3-x} homojunction for the enhancement of both short-range and long-range ion transport. The main process involved in the self-assembly of the Nb–MoO_{3-x} homojunction starting from bulk α-MoO_3 powder has been shown in Figure S1. In general, the bulk layered α-MoO_3 materials were initially converted into 1D nanowires after the solvothermal and probe sonication processes. The similar ionic radii of Mo^{6+} (59 pm) and Nb^{5+} (64 pm) allowed partial substitution of the Nb^{5+} into the Mo^{6+} sites, while preserving the original α-MoO_3 lattice. Furthermore, since the valence state of Nb^{5+} was lower than that of Mo^{6+}, some additional oxygen vacancies could be generated as a consequence of charge balance. Subsequently, those 1D nanowires, which had been partially stacked, formed a nest-like nanostructure as a result of their self-assembly behavior. The self-assembly behavior of those 1D nanowires could be promoted during spray coating, resulting in the formation of numerous stacked nest-like nanostructures due to the *Marangoni* effect.[29] Finally, those stacked nest-like nanostructures could be crystallization driven and self-assembled to grow into 2D nanosheets after annealing at 350°C.[30,31] It is noteworthy that the abundant 1D nanowires persisted following the crystallization process. SEM images of those films after annealing at 100°C and 500°C were shown in Figure S2. It can be seen that, compared to the film annealed at 350°C, an excessively high annealing temperature will cause degradation of the 1D nanowires and coarsening of the 2D nanosheets, while an excessively low annealing temperature is insufficient to form 2D nanosheets. Therefore, the annealing temperature of 350°C is suitable for forming 1D/2D homojunctions.

In order to validate the formation of the Nb–MoO_{3-x} homojunction, transmission electron microscopy (TEM) images of the Nb–MoO_{3-x} nanowires were first presented in Figures 1B and 1C following the solvothermal and probe sonication processes. The two morphologies, including 1D nanowires and a nest-like

CellPress
OPEN ACCESS

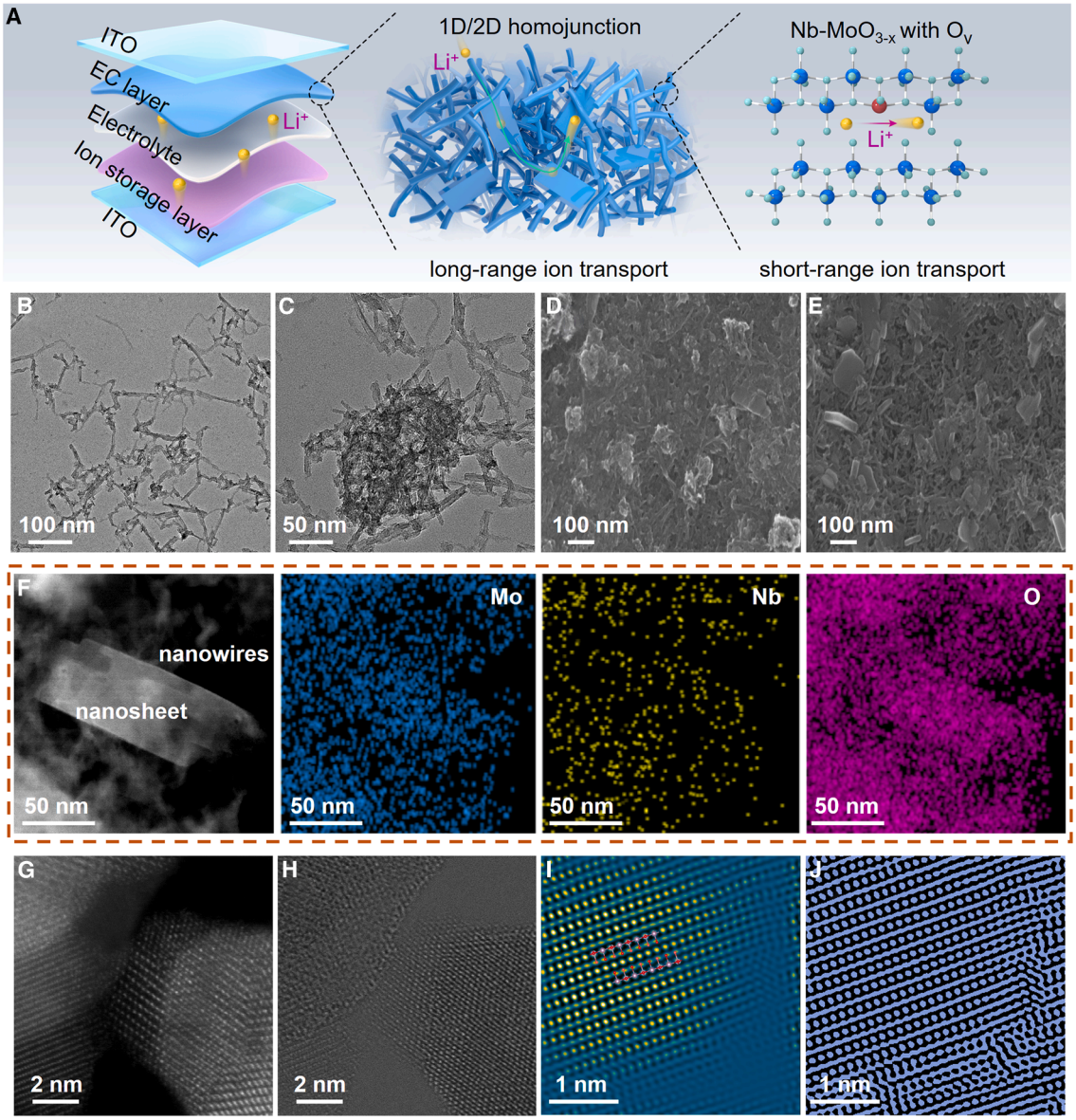


Figure 1. Design and characterization of the Nb–MoO_{3-x} homojunction

(A) Design concept of the Nb–MoO_{3-x} homojunction for the enhancement of short-range and long-range ion transport.
(B) TEM images of 1D nanowire.
(C) TEM images of nest-like nanostructures.
(D) SEM image of the Nb–MoO_{3-x} film after spray coating.
(E) SEM image of the Nb–MoO_{3-x} film after annealing at 350°C.
(F) TEM image of the Nb–MoO_{3-x} homojunction and corresponding EDS mapping of Mo, Nb, and O elements.
(G–J) High-resolution TEM and atomic images of the Nb–MoO_{3-x} in the region of lattice distortion.

nanostructure, have been revealed clearly. These morphologies exhibited well-crystallized characteristics, with a uniform distribution of Mo, Nb, and O elements, as evidenced by high-resolution TEM (HRTEM) and EDS mapping (Figures S3 and S4). Then, Figure 1D showed an SEM image of the Nb–MoO_{3-x} film after spray coating. A multitude of stacked nest-like nanostructures consisting of 1D nanowires were observed in the unannealed films. Figure 1E showed the SEM image of the Nb–MoO_{3-x} film after annealing at 350°C. The numerous 2D nanosheets originated from those stacked nest-like nanostructures could be observed, while plenty of 1D nanowires still remained. The *in-situ*-formed 1D/2D homojunctions spontaneously evolve into island-bridge connections, which will be capable of promoting the long-range ion transport.

TEM images in Figure 1F provided a clear display of the nanostructure of the 1D/2D homojunctions, where a single nanosheet

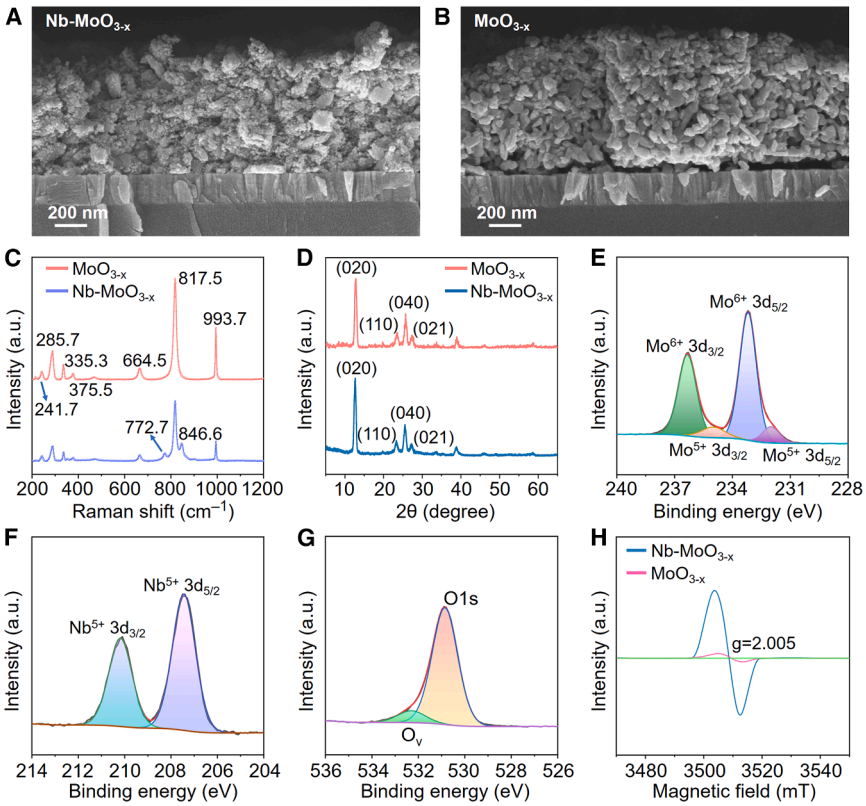


Figure 2. Characterization of the Nb–MoO_{3-x} and pure MoO_{3-x} films

(A and B) SEM cross-sectional images of the prepared films, (A) Nb–MoO_{3-x} and (B) pure MoO_{3-x}.

(C) Raman spectra of the Nb–MoO_{3-x} and pure MoO_{3-x} films.

(D) GIXRD of the Nb–MoO_{3-x} and pure MoO_{3-x} films.

(E–G) The fitted XPS spectra of the Nb–MoO_{3-x} film, (E) Mo 3d; (F) Nb 3d; (G) O 1s.

(H) Electron paramagnetic resonance spectra of the Nb–MoO_{3-x} and pure MoO_{3-x} films.

was surrounded by some nanowires. Moreover, the uniform distribution of Mo, Nb, and O elements was observed in the homojunctions. Corresponding HAADF (high-angle annular dark-field) images were shown in Figure S5 to clearly reveal the overall morphology of the Nb–MoO_{3-x} homojunctions. The elemental contents tested by EDS (Table S1) were close to the designed values, including the amount of Nb doping (about 4% Nb doping). To confirm the doping state of the niobium element, HRTEM images and atomic images of Nb–MoO_{3-x} in the region of lattice distortion were presented in Figures 1G–1J. The core-loss spectrum of EELS (electron energy loss spectroscopy) in Figure S6 indicated the presence of the Nb–MoO_{3-x} homojunction comprising both the lower oxidation state of Mo^{5+} and the highest oxidation state of Nb^{5+}.[32–35] Thus, the region of lattice distortion observed in Figures 1I and 1J was a consequence of Nb^{5+} doping into the lattice of MoO_3, resulting in atomic misalignment. This visual proof demonstrated that Nb doping had occurred in the MoO_3 lattice. As a comparison, the clear atomic images (Figure S7) demonstrated that the distribution of Mo atoms in the sample without Nb doping was regular, while verifying their single-crystal properties through the fast Fourier transform (FFT). The region marked by the red line could be indicative of the (110) plane, with a corresponding lattice spacing of 0.373 nm.

The surface SEM image of the pure MoO_{3-x} film, consisting of nanoparticles, was presented in Figure S8. This image revealed significant differences when compared to the Nb–MoO_{3-x} homojunction. The reason was that charge balance inside the crystal was altered during the Nb doping process, resulting in the formation of lattice distortion and defects.[36] These lattice distortion and defects could facilitate the redistribution of charges and the directional growth of crystals to form 1D nanowires.[37,38] By controlling the same thin-film preparation process and spraying parameters, the thickness of the Nb–MoO_{3-x} homojunction thin film is almost the same as that of the undoped control sample. As illustrated in Figures 2A and 2B, the thickness of both samples was around 830 nm, avoiding the interference of thickness disparity in electrochromic performance comparison. The cross-sectional morphology of the film showed significant differences. For the Nb–MoO_{3-x} homojunction film, 1D nanowires could be filled between 2D nanosheets to form robust frameworks, which were beneficial for contacting with the ITO substrates to avoid film detachment. In contrast, pure MoO_{3-x} films were formed by the relatively loose stacking of nanoparticles, which would be prone to detachment from the ITO substrates.

Raman spectroscopy was shown in Figure 2C. The intrinsically strong peaks near 286, 817, and 994 cm^{-1} could be attributed to the typical characteristic peaks of α-MoO_3 material.[39] The strong Raman band at 817 cm^{-1} was a symmetric stretching mode (Mo–O–Mo) of the double-ligand bridging oxygen, which was a result of the shared angular oxygen of the two octahedra.[40] The 994 cm^{-1} band was the asymmetric stretch of the terminal oxygen atom mode along the *a* and *b* directions, which resulted from an unshared oxygen, and it was assigned to the layered structure of α-MoO_3.[40,41] The wagging mode of the terminal (O=Mo=O) group at the 286 cm^{-1} band was polarized parallel to the *c* direction, reflecting the symmetry-breaking introduced by the oxygen defects.[42] Both Nb–MoO_{3-x} and pure MoO_{3-x} exhibited strong Raman peaks corresponding to the typical α-MoO_3, indicating that they had the same crystal structure as α-MoO_3. The Nb–MoO_{3-x} film exhibited slightly red-shifted peaks compared to the pure MoO_{3-x} film due to the presence of more oxygen vacancies.[43] Besides, the presence of additional bands at 772.7 and 846.6 cm^{-1} in the Raman spectrum of Nb–MoO_{3-x} was indicative of the formation of additional niobium-oxygen bonds. The corner-shared octahedral NbO_6 formed a Nb–O–Nb

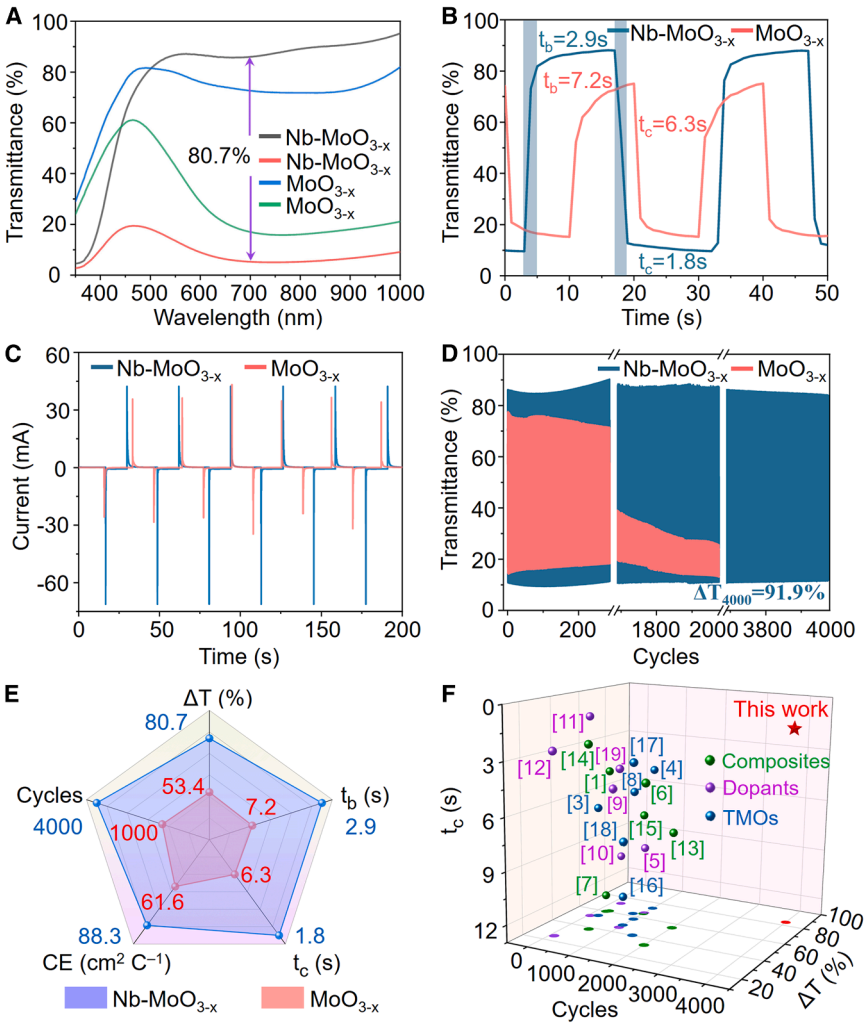


Figure 3. Electrochromic performance of the Nb–MoO_{3-x}//PB and MoO_{3-x}//PB devices

(A) Transmittance of the Nb–MoO_{3-x}//PB and MoO_{3-x}//PB devices in the bleached and colored states.

(B) Comparison of the *in situ* transmittance curves between the Nb–MoO_{3-x}//PB and MoO_{3-x}//PB devices.

(C) Comparison of the *in situ* chronoamperometry curves between the Nb–MoO_{3-x}//PB and MoO_{3-x}//PB devices.

(D) Electrochromic stability of the Nb–MoO_{3-x}//PB and MoO_{3-x}//PB devices.

(E) Comparison of the comprehensive performance between the Nb–MoO_{3-x}//PB and MoO_{3-x}//PB devices.

(F) Comparison of the Nb–MoO_{3-x} with other electrochromic materials in terms of cycling stability, ΔT, and t_c.

collinear bond with a corresponding Raman band appearing near 840 cm^{-1}. The Raman bands observed in the 500–800 cm^{-1} region were characteristic of the stretching modes of the slightly distorted octahedral NbO_6 structures,[44,45] which could be influenced by the presence of nearby Mo–O bonds. Grazing incidence X-ray diffraction (GIXRD) was shown in Figure 2D. The diffraction peaks of both Nb–MoO_{3-x} and pure MoO_{3-x} were consistent with orthorhombic α-MoO_3,[46] which could be indexed to the standard JCPDS no. 75-0912. There was no signal for niobium oxide or other impurity. As shown in Figure S9, compared with MoO_{3-x}, the strongest peak (020) of Nb–MoO_{3-x} shifted to a smaller angle by 0.2°, which means that the Nb–MoO_{3-x} crystal has slightly expanded, and the increase in lattice gap will be beneficial for ion transport.

XPS was conducted to study the chemical composition of samples. Except for the distinct binding energies of Nb 3d and Nb 3p (Nb $3p_{1/2}$ and Nb $3p_{3/2}$), the binding energies of Nb–MoO_{3-x} were consistent with those of pure MoO_{3-x} (Figure S10). Figure 2E revealed the XPS spectrum of the Mo 3d in the Nb–MoO_{3-x} film, which could be deconvoluted into a dual state. The valence states at 233.2 and 236.3 eV could be attributed to Mo $3d_{5/2}$ and Mo $3d_{3/2}$ of Mo^{6+} in the Nb–MoO_{3-x},[47] respectively. The other two valence states at 232.1 and 234.9 eV corresponded to Mo $3d_{5/2}$ and Mo $3d_{3/2}$ of Mo^{5+}.[48] As shown in Figure 2F, the valence states at 207.5 and 210.2 eV could be attributed to Nb $3d_{5/2}$ and Nb $3d_{3/2}$ of Nb^{5+}, indicating the existence of Nb^{5+} in the Nb–MoO_{3-x} homojunction. Figure 2G exhibited the XPS spectrum of the O 1s, which could be separated into two distinguishable peaks with centers at 530.9 and 532.3 eV. The main peak at 530.9 eV was related to the lattice oxygen. Another peak that appeared at 532.3 eV could be regarded as indicative of oxygen vacancies, causing unsaturated coordination around the Mo atom.[49,50] As a contrast, the fitted XPS spectra of the Mo 3d and O 1s in the pure MoO_{3-x} film (Figure S11) showed that the intensity of the Mo^{5+} peaks and oxygen vacancies were weaker than those observed in the Nb–MoO_{3-x} film. The relative content of oxygen vacancies in the Nb–MoO_{3-x} film was approximately 13.3%, higher than that (only 6.7%) of the pure MoO_{3-x} film. The increased presence of oxygen vacancies in the Nb–MoO_{3-x} film is attributed to the effects of Nb^{5+} doping, which could cause charge redistribution, thereby ensuring the overall charge balance of the material. Electron paramagnetic resonance (EPR) could also verify the presence of oxygen vacancies in the Nb–MoO_{3-x} and pure MoO_{3-x}. As illustrated in Figure 2H, the EPR signal peak of the Nb–MoO_{3-x} was much stronger than that of the pure MoO_{3-x} sample. It suggested that the Nb–MoO_{3-x} was capable of producing more lone pair electrons and creating more oxygen vacancies, which was consistent with the XPS analysis.

Figure 3A illustrated the transmittance modulation of both the Nb–MoO_{3-x} and MoO_{3-x} assembled with a Prussian blue (PB) film. It could be observed that the Nb–MoO_{3-x}//PB device in

the bleached state exhibited a high transmittance across the visible and near-infrared wavelength range, while presenting a low transmittance in the colored state. The transmittance modulation of the Nb–MoO_{3-x}//PB electrochromic device at 700 nm (ΔT = 80.7%) was considerably larger than that of the pure MoO_{3-x}//PB device (ΔT = 52.3%), indicating that more lithium ions were injected into the Nb–MoO_{3-x} film at the same bias. In addition, the voltage-dependent ultraviolet-visible (UV-vis) measurements for Nb–MoO_{3-x} and MoO_{3-x} films had been tested to quantify the optical modulation in the device (Figure S12). The excellent optical modulation of the Nb–MoO_{3-x}//PB device was mainly attributed to the Nb–MoO_{3-x} film. Then, as illustrated in Figure S13, the transmittance modulation for the Nb–MoO_{3-x}// PB device was also investigated to reveal the electrochromic performance of the device at different voltages. Figure 3B showed the transmittance fluctuations of the two devices at 700 nm by applying voltage between 2.5 and −2.5 V periodically. The stable optical switching with a large transmittance modulation of 78.6% can be observed in the Nb–MoO_{3-x}//PB electrochromic device with coloring for 15 s and bleaching for 15 s per cycle. The coloring and bleaching response time was defined as the time calculated for about 90% transmittance modulation between colored and bleached states. The Nb–MoO_{3-x}//PB electrochromic device presented a prompt response with coloring time (t_c = 1.8 s) and bleaching time (t_b = 2.9 s). In comparison, the MoO_{3-x}//PB electrochromic device exhibited relatively slower coloring time (t_c = 6.3 s) and bleaching time (t_b = 7.2 s) while maintaining a smaller transmittance modulation (55.3%). The aforementioned switching rate in the electrochromic device is based on the size of 1.5 × 1.5 cm^2.

The coloration efficiency (CE) could be defined as the changes in optical density (ΔOD) per unit charge density (ΔQ) inserted into or extracted from the electrochromic film per unit area. It could be calculated as the following formula[51]:

$$CE = \Delta OD / \Delta Q = log\left(T_b/T_c\right) / \Delta Q, \qquad \text{(Equation 1)}$$

where T_b and T_c represent the transmittance of the electrochromic device in the bleached and colored states, respectively. The ΔQ can be determined by measuring the area of the device and current integration of the corresponding chronoamperometry curves as shown in Figure 3C. The calculated CE at a wavelength of 700 nm for the Nb–MoO_{3-x}//PB electrochromic device was about 88.3 cm^2 C^{-1}, which was higher than that of the MoO_{3-x}//PB electrochromic device (61.6 cm^2 C^{-1}). The higher CE for the Nb–MoO_{3-x}//PB indicated that per unit charge density would cause a larger change in optical density, revealing that the Nb–MoO_{3-x}//PB device could cause a larger optical modulation.[52] Furthermore, the cyclic stability of the Nb–MoO_{3-x}//PB and MoO_{3-x}//PB electrochromic devices was presented in Figure 3D. Following 4,000 cycles, the Nb–MoO_{3-x}//PB electrochromic device retained 91.9% of its initial ΔT, while the MoO_{3-x}//PB electrochromic device only retained 20.9% of its initial ΔT after 2,000 cycles. Therefore, the Nb–MoO_{3-x}//PB device exhibited superior long-term stability to lithium ions in comparison to the MoO_{3-x}//PB device. As illustrated in Figure S14, in addition to the degradation of nanosheets, the Nb–MoO_{3-x} homojunction can still maintain a relatively intact morphology after cycling. In contrast, the morphology of MoO_{3-x} underwent more degeneration after cycling, and the presence of visible cracks may lead to reduced contact with the ITO substrate, which will ultimately affect cycling stability (Figure S15). To visually compare the electrochromic performance of the samples, the overall electrochromic index has been directly presented in Figure 3E. Obviously, by adopting the Nb–MoO_{3-x} homojunction scheme, the electrochromic performance of molybdenum oxide is comprehensively improved. Furthermore, the principal electrochromic performance (cycling stability, ΔT, and t_c) of the Nb–MoO_{3-x} homojunctions exhibited competitive advantages in comparison with other electrochromic metal oxides and their composites, as illustrated in Figure 3F (supported by Table S2).

As illustrated in Figures 4A and 4B, the cyclic voltammetry (CV) curves for the Nb–MoO_{3-x} and MoO_{3-x} films were measured with a potential ranging from −0.6 to 0.9 V vs. silver (Ag) wire. The enclosed area of each CV curve increases as the scan rate increases, indicating the ideal capacitance characteristics. The fitted ion diffusion coefficient D, which represented the kinetics of ion insertion/extraction during the electrochromic process, could be calculated from the scanning-rate-dependent CV measurements. Figure 4C directly revealed that the peak current density of the Nb–MoO_{3-x} and MoO_{3-x} films was a function of (scan rate)$^{1/2}$. Then, the diffusion coefficient (D) of the lithium ions could be calculated using the *Randles-Sevcik* equation as follows[53]:

$$j_p = 2.72 \times 10^5 \times D^{1/2} \times n^{3/2} \times C_0 \times v^{1/2}, \qquad \text{(Equation 2)}$$

where j_p is the peak current density (mA cm^{-2}) of the sample, D is the diffusion coefficient in the unit of cm^2 s^{-1}, n is the number of electrons considered to be 1 for Li^+ ions, C_0 is the concentration of the electrolyte solution (mol cm^{-3}), and v is the scan rate (V s^{-1}). D_{NM} referred to the diffusion coefficient of Li^+ ions in the Nb–MoO_{3-x}, while D_M referred to the diffusion coefficient of Li^+ ions in the MoO_{3-x}. The calculated D_{NM} was about 2.75 × 10^{-10} cm^2 s^{-1}, which was higher than D_M (6.56 × 10^{-11} cm^2 s^{-1}). This directly proves the superior short-range ion transport in the Nb–MoO_{3-x} homojunction compared to the MoO_{3-x} control sample.

To further confirm the capacitive contribution of the current response (i) at a certain voltage (V), the corresponding capacitive contribution and diffusion-controlled behaviors in the CV were measured and calculated by the following equation[54]:

$$i(V) = k_1 v + k_2 v^{1/2}, \qquad \text{(Equation 3)}$$

where k_1v and $k_2v^{1/2}$ represent the intercalation capacitive contribution and diffusion-controlled process, respectively. Compared to the MoO_{3-x} film, the Nb–MoO_{3-x} film exhibited a characteristic of intercalation pseudo-capacitance with the larger current density, suggesting that Nb^{5+} doping could boost the interactions of lithium ions with the electrochromic materials (Figure S16).[55] As shown in Figures 4D and 4E, the fraction of capacitive contribution gradually increased from 73.5% at 1 mV s^{-1} to 85.6% at 5 mV s^{-1} for the Nb–MoO_{3-x} film, while the corresponding fraction of capacitive contribution only increased from 61.5% at 1 mV s^{-1} to 78.2% at 5 mV s^{-1} for the MoO_{3-x} film. Furthermore, the property for the ion transport could also be revealed by the electrochemical impedance

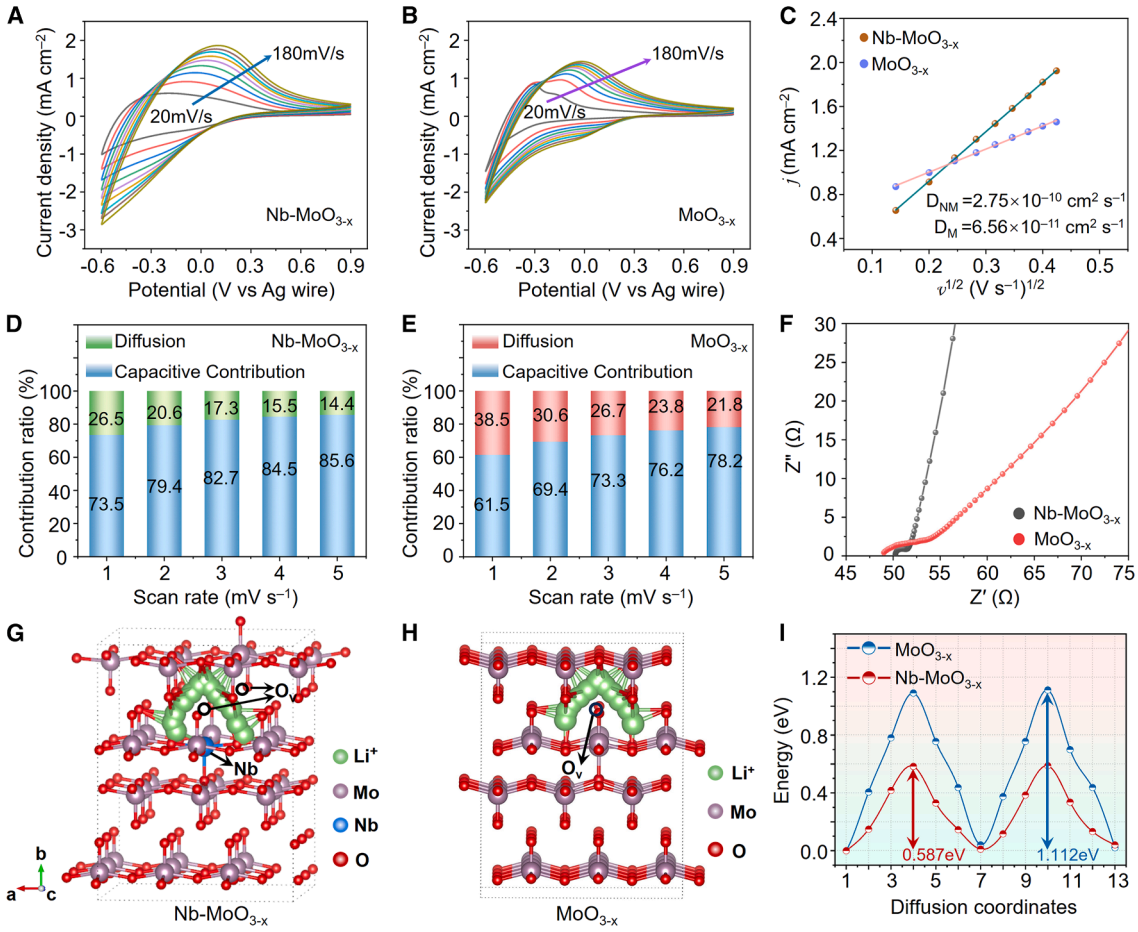


Figure 4. Electrochemical performance and DFT calculation

(A and B) Cyclic voltammetric curves of the prepared film at scan rates from 20 to 180 mV s^{-1}, (A) Nb–MoO_{3-x} and (B) MoO_{3-x}.

(C) Comparison of the lithium-ion diffusion coefficient between the Nb–MoO_{3-x} and MoO_{3-x} films.

(D and E) Distinguished capacitive and diffusion-controlled contributions at slow scan rates from 1 to 5 mV s^{-1} for the prepared films, (D) Nb–MoO_{3-x} and (E) MoO_{3-x}.

(F) Electrochemical impedance spectroscopy of the Nb–MoO_{3-x} and MoO_{3-x} films.

(G and H) DFT models during the process of lithium-ion transport, (G) Nb–MoO_{3-x} and (H) MoO_{3-x}.

(I) Comparison of diffusion energy between the MoO_{3-x} and Nb–MoO_{3-x} during lithium-ion migration.

spectroscopy (EIS) analysis, which would be related to the charge transfer kinetics. The relevant Nyquist plots showed that the Nb–MoO_{3-x} film had a smaller charge-transfer resistance than the MoO_{3-x} film, which accounted for the enhanced ion transport kinetics of the Nb–MoO_{3-x}, as illustrated in Figure 4F. In order to further investigate the influence of Nb doping on the lithium-ion migration within MoO_{3-x}, the corresponding DFT calculations were performed. A crystal model of Nb–substituted Mo sites was constructed on the basis of TEM and EELS analysis. Figure 4G showed a side-view model of the Nb–MoO_{3-x} during the lithium-ion diffusion process, while the MoO_{3-x} model was presented in Figure 4H. As shown in Figure 4I, Li^+ ions diffused from one site to another in the pure MoO_{3-x}, suffering a higher energy barrier of 1.112 eV. However, the calculation results of the Nb–MoO_{3-x} model show a much lower energy barrier of only 0.587 eV. Figure 4I indicated that the diffusion of lithium ions in the Nb–MoO_{3-x} was a more feasible process, due to the facilitated short-range ion transport, thereby enhancing the electrochromic performance.

In addition to the improvement at the lattice scale, the unique one-dimensional and two-dimensional composite morphology of the Nb–MoO_{3-x} homojunction also facilitates ion transport over a relatively larger range. During the electrochromic process, the major difference in the long-range ion transport between Nb–MoO_{3-x} and MoO_{3-x} was shown in Figure S17. Thanks to the interconnected nanowires and nanosheets in the Nb–MoO_{3-x} homojunction, Li^+ ions can rapidly migrate throughout the entire electrochromic layer. Compared with the MoO_{3-x} control sample, the interconnected island-bridge structure in the Nb–MoO_{3-x} homojunction provides more paths and active sites for charge transfer. At the same time, it also brings better structural stability by buffering lattice

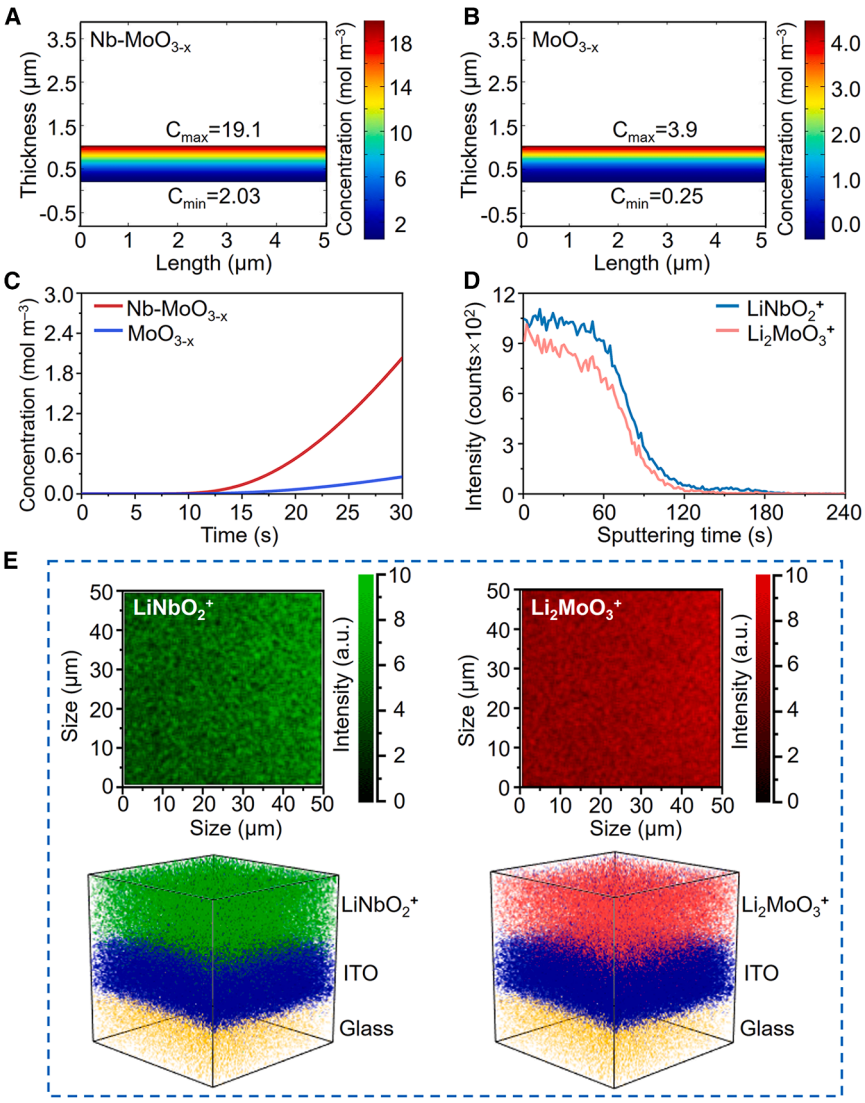


Figure 5. COMSOL simulation and characterization of TOF-SIMS

(A and B) Lithium-ion concentration distribution inside the film, (A) Nb–MoO_{3-x} and (B) MoO_{3-x}.

(C) Lithium-ion concentration within the Nb–MoO_{3-x} and MoO_{3-x} films over time.

(D) Main composition of the lithium-ion-inserted Nb–MoO_{3-x} film.

(E) 2D mapping and reconstructed 3D images of the TOF-SIMS secondary ion fragments sputtered from the lithium-ion-inserted Nb–MoO_{3-x} film with an electrochromic colored state. The sputtered area is 50 μm × 50 μm.

expansion stress during ion insertion and extraction. These factors related to long-range ion transport have brought about a comprehensive improvement of electrochromic performance. To further validate the aforementioned analysis, the kinetics mechanism of long-range ion transport inside the electrochromic film was investigated by using simulation analysis (COMSOL Multiphysics). The Nb–MoO_{3-x} film provided optimized transport channels of ions, which was beneficial for the combination with electrons to produce an electrochromic redox reaction.[56,57] As illustrated in Figures 5A and 5B, the 2D spatial distribution of the Nb–MoO_{3-x} film demonstrated a greater capacity to accommodate lithium ions than that of the pure MoO_{3-x} film across the entire region. The simulation result in Figure 5C demonstrated the variations in lithium-ion concentration over the entire coloring period (30 s) at the same depth of the film for the Nb–MoO_{3-x} and pure MoO_{3-x} models. Compared to the pure MoO_{3-x}, the concentration of lithium ions in the Nb–MoO_{3-x} film increased faster, indicating much easier long-range ion transport.

TOF-SIMS (time-of-flight secondary ion mass spectrometry) was employed to chemically characterize the lithium-ion-inserted Nb–MoO_{3-x} film with depth profiles, thereby revealing the spatial distribution of chemical species.[58–60] Figure 5D showed two components of the lithium-ion-inserted Nb–MoO_{3-x} film over sputtering time. Figure 5E presented 2D mapping and reconstructed 3D images of the TOF-SIMS. The intensity distribution of the ITO glass substrate was shown in Figure S18. The results indicated that the intensity signals of the lithium-intercalated niobium compounds and molybdenum compounds were uniformly distributed in space, in accordance with the COMSOL model of long-range lithium-ion transport inside the electrochromic film. From the reconstructed 3D image in Figure 5E, it can be seen that lithium ions penetrate the entire Nb–MoO_{3-x} homojunction layer (reaching the ITO layer along the thickness direction), rather than being limited to the shallow surface. The TOF-SIMS results of the electrochromic sample in the colored state further confirm the excellent long-range ion transport capability of the Nb–MoO_{3-x} homojunctions.

Figure 6A illustrated a large-area (10 × 10 cm^2) electrochromic device based on the Nb–MoO_{3-x}//PB with three modes (dark, cool, and bright). The electrochromic smart window shown in Figure 6A was ultimately also operated at 2.5 V. In addition, the electrochromic device could be driven at a low voltage of 1.5 V between the dark and bright modes for achieving the energy-saving purpose (Figure S19). Figure 6B demonstrated the solar radiation modulation of the Nb–MoO_{3-x}//PB device and glass. From the visible to near-infrared wavelength range (400–2,400 nm), the device exhibits minimal absorption of solar radiation when operating in the bright mode. In dark mode, it effectively blocks the majority of solar radiation, thereby demonstrating excellent modulation of solar radiation. To evaluate the heat insulation capability of the Nb–MoO_{3-x}//PB device, we constructed an experimental model

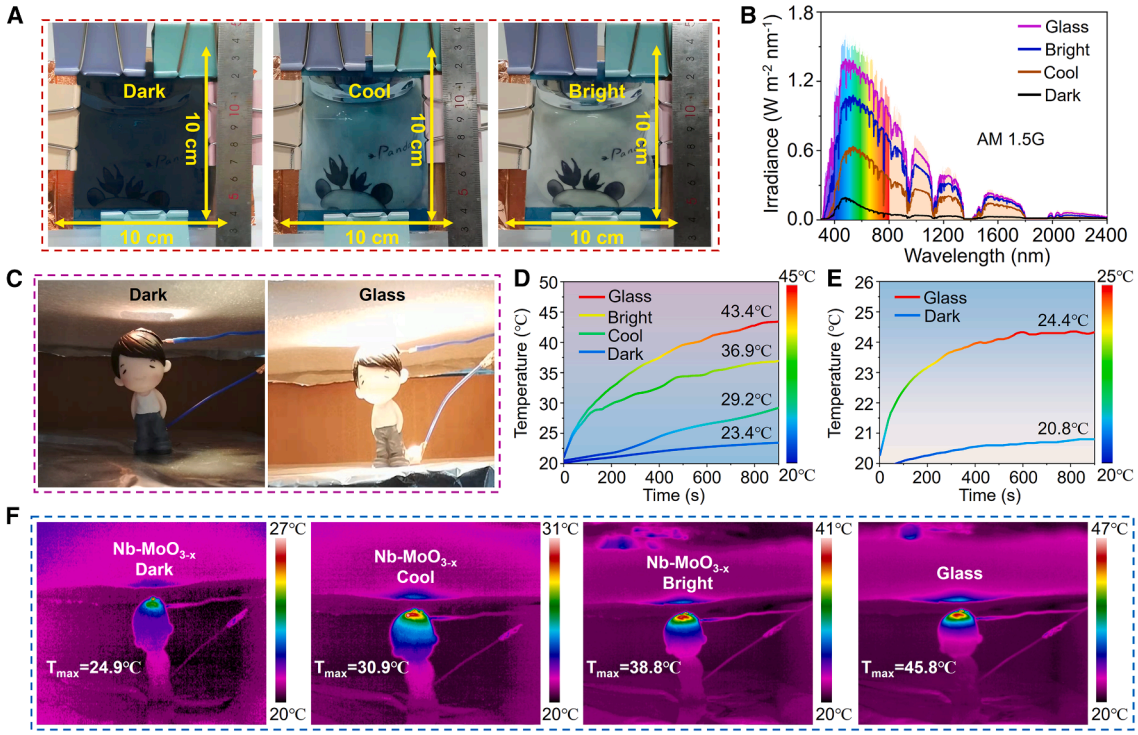


Figure 6. Photographs of a large-area electrochromic device and corresponding heat-insulation performance

(A) Dark, cool, and bright modes of the Nb–MoO_{3-x}//PB device.

(B) Solar irradiation spectra of the Nb–MoO_{3-x}//PB device in three working modes compared with those of glass.

(C) Experimental model with the Nb–MoO_{3-x}//PB electrochromic device under the dark mode and glass.

(D and E) Plot of *in situ* temperature variation derived from the experimental model, (D) top region and (E) bottom region.

(F) Infrared thermal images of the experimental model with the Nb–MoO_{3-x}//PB device and glass.

using an infrared lamp and thermocouples for measurement. The infrared lamp simulated sunlight shining directly on the doll from above, with glass and Nb–MoO_{3-x}//PB devices serving as media to block the infrared radiation. Figure 6C presented photographs of the testing system, including an Nb–MoO_{3-x}//PB electrochromic device under dark mode and glass as the corresponding medium, respectively. The photographs of the cool and bright modes were shown in Figure S20.

To ensure the accuracy of the temperature data, a multi-channel temperature recorder (EX4000) was employed to measure the temperature variation derived from the experimental doll. Figure 6D presented the curves of temperature variation under continuous illumination of 15 min. With the Nb–MoO_{3-x}//PB device (dark mode) as the medium, the temperature had only risen by 3.4°C, significantly lower than that with the ordinary glass (23.4°C). Additionally, Figure 6E illustrated the variation of environmental temperature within this testing system. These results indicate that the Nb–MoO_{3-x}//PB electrochromic device can effectively regulate temperature variation caused by infrared radiation, thereby maintaining the indoor temperature at a comfortable level. The temperature distribution of the experimental doll was also recorded by an infrared thermal imager (FLUKE, TiS 75+), including the dark, cool, and bright modes of the Nb–MoO_{3-x}//PB device and glass, as shown in Figure 6F. The results have clearly demonstrated the excellent heat insulation capability of the Nb–MoO_{3-x}//PB device. The highest temperature recorded for the experimental doll was 45.8°C after 15 min illumination, with the glass as the medium. For comparison, when the Nb–MoO_{3-x}//PB device under dark mode served as the window, the recorded temperature was only 24.9°C. The results indicate that the Nb–MoO_{3-x}//PB device has the potential to serve as the efficient energy-saving window, which will be capable of reducing indoor temperature in summer.

DISCUSSION

A high-performance electrochromic Nb–MoO_{3-x} homojunction composed of 1D nanowires and 2D nanosheets through a facile wet chemical route has been discovered. The experimental results and theoretical calculations reveal that Nb doping with oxygen vacancies can reduce the energy barrier for ion migration within the lattice, thereby increasing the ion diffusion coefficient by an order of magnitude. Meanwhile, the interconnected nanowire-nanosheet architecture within the Nb–MoO_{3-x} homojunction facilitates the rapid Li^+ ion transport throughout the entire electrochromic layer. With the synergistic enhancement of short-range and long-range ion transport, the electrochromic device based on the Nb–MoO_{3-x} homojunction can simultaneously achieve large transmittance modulation (80.7%) and ultrafast electrochromic speed (t_b = 2.9 s, t_c = 1.8 s). The

abundant ion transport pathways and the structural stability of the Nb–MoO_{3-x} homojunction endow the device with a superior cycling stability (91.9% retention after 4,000 cycles), which is the best record in molybdenum oxide. Furthermore, a large-area device with a low driving voltage of 1.5 V and outstanding heat insulation ability has been successfully prepared, verifying its application potential as a smart window. This work provides an easy yet effective strategy to realize a metal oxide homojunction for electrochromic application. The two-stage optimization strategy of element doping and morphology modulation to boost the ion transport can also be referenced in other electrochemical energy storage and conversion fields.

METHODS

Preparation of Nb-doped MoO_{3-x} film

Firstly, 0.23 g of niobium oxalate was dissolved in 40 mL of solvent (20 mL deionized water, 10 mL methanol, and 10 mL diethylene glycol) by continuous magnetic stirring. Meanwhile, 1.44 g of MoO_3 powder was wet ground with 1 mL of deionized water and then dispersed in the aforementioned 40 mL mixture solution. After stirring at room temperature for 2 h, the mixture solution was sonicated for 1 h. Subsequently, the mixture solution was transferred into a Teflon-lined stainless-steel autoclave (50 mL) and treated at 180°C for 8 h. After cooling down to room temperature naturally, the precipitate was collected and washed several times with deionized water by centrifugation at 9,000 r/min for 15 min and then redispersed in the 80 mL mixed solvents (60 mL isopropanol and 20 mL of deionized water) with probe sonicating for about 3 h. Finally, the delaminated suspension was collected after centrifugation at 4,000 r/min for 30 min. The Nb-doped MoO_{3-x} films were prepared by spraying the aforementioned delaminated suspension onto pre-cleaned ITO glass substrates. When spraying the films, the ITO glass substrates were placed on a hot plate at 90°C, which allowed the films to dry immediately after spraying. Finally, the Nb-doped MoO_{3-x} films could be derived after annealing at 350°C for 20 min. As a contrast, the pure MoO_{3-x} films were prepared by the same procedure without niobium oxalate addition.

Electrochemical deposition of PB film

Before the process of electrochemical deposition, the cleaned ITO glass substrates were plasma treated at 50 W for 5 min to make the surface hydrophilic. To prepare the electrodeposition solution, 0.3 g KCl and 0.1 g $K_3Fe(CN)_6$ were dispersed in 35 mL of deionized water, and then 0.05 g $FeCl_3$ and 1 mL HCl (36%) were added into another 35 mL of deionized water and subsequently mixed with the aforementioned solution while stirring thoroughly for about 2 h. The ITO glass was immersed into the aforementioned solution and used as the working electrode, and a Pt electrode was used as a counter electrode. A potentiostatic voltage of 0.7 V was applied by a programmable DC power supply (DP832A, RIGOL) for 60 s. Finally, the as-prepared PB film was washed several times with deionized water to remove the extra solution, followed by drying in air under 105°C for 20 min.

Assembly of electrochromic device

In order to fabricate the electrochromic devices, the Nb–MoO_{3-x} film on the ITO glass, 1 M $LiClO_4$ in a mixed solvent (PC:DMC = 1:1), and the PB film on the ITO glass were used as the electrochromic layer, electrolyte, and ion storage layer. The spacer was sandwiched between the Nb-doped MoO_{3-x} film and the PB film to fix the electrolyte layer and avoid electrolyte leakage. Eventually, all parts were firmly sealed with a double-sided adhesive tape (4910, 3M). As a contrast, the MoO_{3-x} electrochromic devices were prepared by the same procedure; the only difference was that pure MoO_{3-x} films were used as the electrochromic layer.

Electrochemical and electrochromic measurements

The transmittance of the prepared electrochromic device was measured on spectrophotometers (Mapada V-1600PC and Shimadzu UV-3600i Plus). The chronoamperometry curve was obtained by a digital source meter (Keithley 2410). The EIS and CV curves were tested using an electrochemical workstation (Zennium Pro, Zahner, Germany) with a three-electrode system. The ITO glass with electrochromic film, graphite sheet, and the Ag wire were used as the working electrode, counter electrode, and reference electrode, respectively. The results of EIS were obtained over the frequency scope from 100 kHz to 10 mHz with an AC amplitude of 10 mV. The CV curves were recorded within the potential range from −0.6 to 0.9 V vs. Ag wire.

Further details regarding the methods can be found in the supplemental information.

RESOURCE AVAILABILITY

Lead contact

Further information and requests for resources should be directed to and will be fulfilled by the lead contact, Huajing Fang (fanghj@xjtu.edu.cn).

Materials availability

This study did not generate new unique reagents.

Data and code availability

Data and code supporting the findings of this paper are available from the lead contact upon reasonable request.

ACKNOWLEDGMENTS

This work was supported by the National Natural Science Foundation of China (no. 51902250) and Xi'an Key Laboratory for Light Alloys (201805064ZD15CG48). Part of this work was facilitated by the utilization of the advanced electron microscopy facilities housed within the XJTU-NIN-Hitachi Joint Research Center at Xi'an Jiaotong University, China. We would like to acknowledge Xiaofeng Zhang for his assistance with data processing and valuable discussions. We thank the Instrument Analysis Center of Xi'an Jiaotong University for contributions to the materials characterization.

AUTHOR CONTRIBUTIONS

H.Y. and H.F. designed research; H.Y. and K.J. performed research; H.Y., Q.Z., and Y.Q. contributed to materials characterization; H.Y. analyzed the data and wrote the manuscript; and H.F. and Y.C. reviewed the paper.

DECLARATION OF INTERESTS

The authors declare no competing interests.

SUPPLEMENTAL INFORMATION

Supplementary data related to this article can be found online at https://doi.org/10.1016/j.matlit.2026.100137.

Received: June 29, 2026
Revised: August 29, 2026
Accepted: September 8, 2026
Published: September 29, 2026

REFERENCES

1. Cai, G., Wang, J., and Lee, P.S. (2016). Next-Generation Multifunctional Electrochromic Devices. Acc. Chem. Res. *49*, 1469–1476. https://doi.org/10.1021/acs.accounts.6b00183.
2. Jia, Y., Liu, D., Chen, D., Jin, Y., Chen, C., Tao, J., Cheng, H., Zhou, S., Cheng, B., Wang, X., et al. (2023). Transparent dynamic infrared emissivity regulators. Nat. Commun. *14*, 5087. https://doi.org/10.1038/s41467-023-40902-w.
3. Bansal, L., Kaladi Chondath, S., Sahu, B., Rath, D.K., Ahlawat, N., Gupta, A., Saxena, S.K., Lee, P.S., and Kumar, R. (2026). Emerging Multivalent Electrochromic Batteries: Dual-Function Energy Storage with Visual Intelligence. ACS Energy Lett. *11*, 111–124. https://doi.org/10.1021/acsenergylett.5c03306.
4. Thakur, V.K., Ding, G., Ma, J., Lee, P.S., and Lu, X. (2012). Hybrid Materials and Polymer Electrolytes for Electrochromic Device Applications. Adv. Mater. *24*, 4071–4096. https://doi.org/10.1002/adma.201200213.
5. Sheng, S.Z., Wang, J.L., Zhao, B., He, Z., Feng, X.F., Shang, Q.G., Chen, C., Pei, G., Zhou, J., Liu, J.W., and Yu, S.H. (2023). Nanowire-based smart windows combining electro- and thermochromics for dynamic regulation of solar radiation. Nat. Commun. *14*, 3231. https://doi.org/10.1038/s41467-023-38353-4.
6. Shao, Z., Huang, A., Cao, C., Ji, X., Hu, W., Luo, H., Bell, J., Jin, P., Yang, R., and Cao, X. (2024). Tri-band electrochromic smart window for energy savings in buildings. Nat. Sustain. *7*, 796–803. https://doi.org/10.1038/s41893-024-01349-z.
7. Rao, T., Zhou, Y., Jiang, J., Yang, P., and Liao, W. (2022). Low dimensional transition metal oxide towards advanced electrochromic devices. Nano Energy *100*, 107479. https://doi.org/10.1016/j.nanoen.2022.107479.
8. Novak, T.G., Kim, J., Tiwari, A.P., Kim, J., Lee, S., Lee, J., and Jeon, S. (2020). 2D MoO_3 Nanosheets Synthesized by Exfoliation and Oxidation of MoS_2 for High Contrast and Fast Response Time Electrochromic Devices. ACS Sustainable Chem. Eng. *8*, 11276–11282. https://doi.org/10.1021/acssuschemeng.0c03191.
9. Yu, H., Zhao, Q., Bai, J., Li, X., Xu, Y., Feng, Y., Liu, Z., Sun, B., and Fang, H. (2025). Mechanochemical Synthesis of Amorphous MoO_{3-x} Quantum Dots for All-In-One Electrochromic Devices. Adv. Opt. Mater. *13*, e00813. https://doi.org/10.1002/adom.202500813.
10. Fang, H., Zheng, P., Ma, R., Xu, C., Yang, G., Wang, Q., and Wang, H. (2018). Multifunctional hydrogel enables extremely simplified electrochromic devices for smart windows and ionic writing boards. Mater. Horiz. *5*, 1000–1007. https://doi.org/10.1039/c8mh00856f.
11. Huang, S., Zhang, R., Shao, P., Zhang, Y., and Wen, R.T. (2022). Electrochromic Performance Fading and Restoration in Amorphous TiO_2 Thin Films. Adv. Opt. Mater. *10*, 2200903. https://doi.org/10.1002/adom.202200903.
12. Zhang, R., Zhou, Q., Huang, S., Zhang, Y., and Wen, R.T. (2024). Capturing ion trapping and detrapping dynamics in electrochromic thin films. Nat. Commun. *15*, 2294. https://doi.org/10.1038/s41467-024-46500-8.
13. Zhang, R., Huang, Q., Ou, Z., Khan, T.A., Yin, M., Gao, E., Sun, J., and Wen, R.T. (2025). Retaining superior electrochromic performance by effective suppression of ion trapping upon cycling. Mater. Horiz. *12*, 3721–3730. https://doi.org/10.1039/d5mh00229j.
14. Sun, X., Wu, W., Zhao, X., Qu, Z., Xu, K., Zhang, X., Wang, B., Rong, X., Wang, X., Wu, G., and Liu, N. (2025). Metal doping engineering of W18O49 for excellent dual-band electrochromic smart windows with integrated energy storage function. Nano Res. *18*, 94907807. https://doi.org/10.26599/nr.2025.94907807.
15. Guo, X., Jia, S., Li, N., and Cai, G. (2024). Regulating the Ion Transport in the Layered V2O5 (2024). Electrochromic Films with Tunable Interlayer Spacing. Adv. Opt. Mater. *12*, 2400459. https://doi.org/10.1002/adom.202400459.
16. Heo, S., Cho, S.H., Dahlman, C.J., Agrawal, A., and Milliron, D.J. (2020). Influence of Crystalline and Shape Anisotropy on Electrochromic Modulation in Doped Semiconductor Nanocrystals. ACS Energy Lett. *5*, 2662–2670. https://doi.org/10.1021/acsenergylett.0c01236.
17. Bansal, L., Sahu, B., Rath, D.K., Ahlawat, N., Ghosh, T., Kandpal, S., and Kumar, R. (2024). Stoichiometrically Optimized Electrochromic Complex $[V_2O_{2+\xi}(OH)_{3-\xi}]$ Based Electrode: Prototype Supercapacitor with Multicolor Indicator. Small *20*, 2312215. https://doi.org/10.1002/smll.202312215.
18. Liu, Y., Cao, S., Su, Y., Bao, L., Liang, R., Liang, Y., Li, Y., Cai, D., and Zou, B. (2026). Ultra-Stable Dual-Band Electrochromic Windows Enabled by Shear-Phase Niobium Oxide. Adv. Energy Mater. *16*, e05972. https://doi.org/10.1002/aenm.202505972.
19. Zhao, F., Chen, Y., Shi, G., Liu, Q., Liu, Y., and Han, G. (2025). Revealing the Mechanism of Ni Vacancies on Ion Storage, Diffusion Kinetics, and Electrochromic Performance of Nickel Oxide Electrodes. Small *21*, 2411995. https://doi.org/10.1002/smll.202411995.
20. Chen, M., Deng, J., Zhang, H., Zhang, X., Yan, D., Yao, G., Hu, L., Sun, S., Zhao, J., and Li, Y. (2025). Advanced Dual-Band Smart Windows: Inorganic All-Solid-State Electrochromic Devices for Selective Visible and Near-Infrared Modulation. Adv. Funct. Mater. *35*, 2413659. https://doi.org/10.1002/adfm.202413659.
21. Tang, S., Niu, J., Gu, C., Zhang, H., Zheng, R., Weng, X., and Jia, C. (2024). VIS–IR electrochromic device with electromagnetic wave absorption function based on a Fe_3O_4@PANI composite material. J. Mater. Chem. C *12*, 10621–10634. https://doi.org/10.1039/d4tc02018a.
22. Liu, Y., Yuan, J., Wang, Y., Zheng, R., Liu, Q., Shang, X., Shao, J., Wan, Z., Luo, J., and Jia, C. (2023). Approach to Significantly Enhancing the Electrochromic Performance of PANi by In Situ Electrodeposition of the PANi@MXene Composite Film. ACS Appl. Mater. Interfaces *15*, 58940–58954. https://doi.org/10.1021/acsami.3c15548.
23. Hsu, S.C., Chao, S.H., Wu, N.J., Huang, J.H., Kang, J.L., Weng, H.C., and Liu, T.Y. (2023). Facile synthesis of hybrid WO_3/MoO_x electrochromic films for application in complementary electrochromic devices. J. Alloys Compd. *945*, 169256. https://doi.org/10.1016/j.jallcom.2023.169256.
24. Lou, J., Zhu, X., Li, T., Yang, X., Ma, D., Zhu, L., and Wang, J. (2024). Preparation and Electrochromic Properties of MnO_2/PPy Composite Films with Coral-like Structures. ACS Appl. Mater. Interfaces *16*, 36942–36952. https://doi.org/10.1021/acsami.4c05669.
25. Hassan, M., Ghaffar, A., Lou, G., Miao, Z., Peng, Z., and Celebi, K. (2024). Enhanced Transport Kinetics of Electrochromic Devices by $W_{18}O_{49}$ NW/$Ti_3C_2T_x$ Composite Films. Adv. Funct. Mater. *34*, 2310535. https://doi.org/10.1002/adfm.202310535.
26. Yu, H., Fang, H., Jing, K., Ma, H., Wu, L., and Chai, Y. (2024). Electrochromic Devices based on 2D MoO_{3-x}/PEDOT: PSS Composite Film with Boosted Ion Transport. ACS Appl. Mater. Interfaces *16*, 18052–18062. https://doi.org/10.1021/acsami.4c01108.
27. Tang, Y., Yuan, J., Zheng, R., and Jia, C. (2026). Scalable Fabrication of Large-Scale Electrochromic Smart Windows for Superior Solar Radiation Regulation and Energy Savings. Nano-Micro Lett. *18*, 211. https://doi.org/10.1007/s40820-025-02055-x.

28. Wang, F., Pei, K., Li, Y., Li, H., and Zhai, T. (2021). 2D Homojunctions for Electronics and Optoelectronics. Adv. Mater. *33*, 2005303. https://doi.org/10.1002/adma.202005303.

29. Li, H., Mcrae, L., Firby, C.J., and Elezzabi, A.Y. (2019). Rechargeable aqueous electrochromic batteries utilizing Ti-substituted tungsten molybdenum oxide based Zn^{2+} ion intercalation cathodes. Adv. Mater. *31*, 1807065. https://doi.org/10.1002/adma.201807065.

30. Shi, Z., Wei, Y., Zhu, C., Sun, J., and Li, Z. (2018). Crystallization-driven two-dimensional nanosheet from hierarchical self-assembly of polypeptoid-based diblock copolymers. Macromolecules *51*, 6344–6351. https://doi.org/10.1021/acs.macromol.8b00986.

31. Jia, S., Zheng, H., Sang, H., Zhang, W., Zhang, H., Liao, L., and Wang, J. (2013). Self-assembly of K_xWO_3 nanowires into nanosheets by an oriented attachment mechanism. ACS Appl. Mater. Interfaces *5*, 10346–10351. https://doi.org/10.1021/am403414a.

32. Hanson, E.D., Lajaunie, L., Wolverton, C., Arenal, R., and Dravid, V.P. (2017). Systematic study of oxygen vacancy tunable transport properties of few-layer MoO_{3-x} enabled by vapor-based synthesis. Adv. Funct. Mater. *27*, 1605380. https://doi.org/10.1002/adfm.201605380.

33. Huang, W., Deng, K., Wei, Q., and Zhou, Y. (2024). Atomic-scale structural evolution and characterization of molybdenum carbide nanoparticles grown from MoO_3 and MoS_2: high-resolution in situ ETEM and EELS. Cryst. Growth Des. *24*, 522–531. https://doi.org/10.1021/acs.cgd.3c01196.

34. Bach, D., Schneider, R., Gerthsen, D., Verbeeck, J., and Sigle, W. (2009). EELS of niobium and stoichiometric Niobium-oxide phases—Part I: Plasmon and near-edges fine structure. Microsc. Microanal. *15*, 505–523. https://doi.org/10.1017/S1431927609990105X.

35. Li, X., Jiang, Y., Jin, Q., Qin, F., Yao, T., Tao, A., Yan, X., Gao, C., Yang, Z., Chen, C., et al. (2025). Nb-doped coherent $TiO_2/LaAlO_3$ interfaces: Segregation mechanism and improved photocatalytic performance. Acta Mater. *282*, 120504. https://doi.org/10.1016/j.actamat.2024.120504.

36. Lu, Q., Huang, B., Zhang, Q., Chen, S., Gu, L., Song, L., Yang, Y., and Wang, X. (2021). Single-crystal inorganic helical architectures induced by asymmetrical defects in sub-nanometric wires. J. Am. Chem. Soc. *143*, 9858–9865. https://doi.org/10.1021/jacs.1c03607.

37. Insua, I., and Montenegro, J. (2020). 1D to 2D Self assembly of cyclic peptides. J. Am. Chem. Soc. *142*, 300–307. https://doi.org/10.1021/jacs.9b10582.

38. Lin, Y., Thomas, M.R., Gelmi, A., Leonardo, V., Pashuck, E.T., Maynard, S.A., Wang, Y., and Stevens, M.M. (2017). Self-assembled 2D free-standing Janus nanosheets with single layer thickness. J. Am. Chem. Soc. *139*, 13592–13595. https://doi.org/10.1021/jacs.7b06591.

39. Hou, X., Ruan, M., Zhou, L., Wu, J., Meng, B., Huang, W., Zhong, K., Yang, K., Fang, Z., and Xie, K. (2023). Superior lithium storage performance in MoO_3 by synergistic effects: Oxygen vacancies and nanostructures. J. Energy Chem. *78*, 91–101. https://doi.org/10.1016/j.jechem.2022.11.011.

40. Dwivedi, C., Mohammad, T., Bharti, V., Patra, A., Pathak, S., and Dutta, V. (2018). CoSP approach for the synthesis of blue MoO_3 nanoparticles for application as hole transport layer (HTL) in organic solar cells. Sol. Energy *162*, 78–83. https://doi.org/10.1016/j.solener.2017.12.063.

41. Jittiarporn, P., Sikong, L., Kooptarnond, K., Taweepreda, W., Stoenescu, S., Badilescu, S., and Truong, V.V. (2017). Electrochromic properties of MoO_3-WO_3 thin films prepared by a sol-gel method, in the presence of a triblock copolymer template. Surf. Coat. Technol. *327*, 66–74. https://doi.org/10.1016/j.surfcoat.2017.08.012.

42. Yan, B., Zheng, Z., Zhang, J., Gong, H., Shen, Z., Huang, W., and Yu, T. (2009). Orientation controllable growth of MoO_3 nanoflakes: Micro-Raman, field emission, and birefringence properties. J. Phys. Chem. C *113*, 20259–20263. https://doi.org/10.1021/jp907602w.

43. Liu, H., Cai, Y., Han, M., Guo, S., Lin, M., Zhao, M., Zhang, Y., and Chi, D. (2018). Aqueous and mechanical exfoliation, unique properties, and theoretical understanding of MoO_3 nanosheets made from free-standing α-MoO_3 crystals: Raman mode softening and absorption edge blue shift. Nano Res. *11*, 1193–1203. https://doi.org/10.1007/s12274-017-1733-x.

44. Jehng, J.M., and Wachs, I.E. (1991). Structural chemistry and Raman spectra of Niobium oxides. Chem. Mater. *3*, 100–107. https://doi.org/10.1021/cm00013a025.

45. Meng, J., He, Q., Xu, L., Zhang, X., Liu, F., Wang, X., Li, Q., Xu, X., Zhang, G., Niu, C., et al. (2019). Identification of phase control of carbon-confined Nb_2O_5 nanoparticles toward high-performance lithium storage. Adv. Energy Mater. *9*, 1802695. https://doi.org/10.1002/aenm.201802695.

46. Illyaskutty, N., Sreedhar, S., Sanal Kumar, G., Kohler, H., Schwotzer, M., Natzeck, C., and Pillai, V.P.M. (2014). Alteration of architecture of MoO_3 nanostructures on arbitrary substrates: growth kinetics, spectroscopic and gas sensing properties. Nanoscale *6*, 13882–13894. https://doi.org/10.1039/c4nr04529g.

47. Yu, M., Shao, H., Wang, G., Yang, F., Liang, C., Rozier, P., Wang, C.Z., Lu, X., Simon, P., and Feng, X. (2020). Interlayer gap widened α-phase molybdenum trioxide as high-rate anodes for dual-ion intercalation energy storage devices. Nat. Commun. *11*, 1348. https://doi.org/10.1038/s41467-020-15216-w.

48. Li, N., Li, Y., Sun, G., Ma, Y., Chang, T., Ji, S., Yao, H., Cao, X., Bao, S., and Jin, P. (2017). Selective and tunable near-infrared and visible light transmittance of MoO_{3-x} nanocomposites with different crystallinity. Chem. Asian J. *12*, 1709–1714. https://doi.org/10.1002/asia.201700437.

49. Shen, S., Zhang, X., Cheng, X., Xu, Y., Gao, S., Zhao, H., Zhou, X., and Huo, L. (2019). Oxygen-vacancy-enriched porous α-MoO_3 nanosheets for trimethylamine sensing. ACS Appl. Nano Mater. *2*, 8016–8026. https://doi.org/10.1021/acsanm.9b02072.

50. Zhuiykov, S., Kats, E., Carey, B., and Balendhran, S. (2014). Proton intercalated two-dimensional WO_3 nano-flakes with enhanced charge-carrier mobility at room temperature. Nanoscale *6*, 15029–15036. https://doi.org/10.1039/c4nr05008h.

51. Zhou, J., Wei, Y., Luo, G., Zheng, J., and Xu, C. (2016). Electrochromic properties of vertically aligned Ni-doped WO_3 nanostructure films and their application in complementary electrochromic devices. J. Mater. Chem. C *4*, 1613–1622. https://doi.org/10.1039/c5tc03750f.

52. Li, R., Ma, X., Li, J., Cao, J., Gao, H., Li, T., Zhang, X., Wang, L., Zhang, Q., Wang, G., et al. (2021). Flexible and high-performance electrochromic devices enabled by self-assembled 2D TiO_2/MXene heterostructures. Nat. Commun. *12*, 1587. https://doi.org/10.1038/s41467-021-21852-7.

53. Wu, W., Fang, H., Ma, H., Wu, L., Zhang, W., and Wang, H. (2020). Boosting transport kinetics of ions and electrons simultaneously by $Ti_3C_2T_x$ (MXene) addition for enhanced electrochromic performance. Nano-Micro Lett. *13*, 20. https://doi.org/10.1007/s40820-020-00544-9.

54. Wang, C., Zhao, C., Pu, X., Zeng, Y., Wei, Y., Cao, Y., and Chen, Z. (2024). Sulfur-Defect-Induced $TiS_{1.94}$ as a high-capacity and long-life anode material for Zinc-ion batteries. ACS Appl. Mater. Interfaces *16*, 17637–17648. https://doi.org/10.1021/acsami.4c01311.

55. Yu, X., Zhao, G., Liu, C., Wu, C., Huang, H., He, J., and Zhang, N. (2021). A MoS_2 and graphene alternately stacking van der Waals heterostructure for Li^+/Mg^{2+} co-intercalation. Adv. Funct. Mater. *31*, 2103214. https://doi.org/10.1002/adfm.202103214.

56. Huo, X., Miao, X., Han, X., Tang, S., Zhang, M., and Guo, M. (2020). High-performance electrochromic supercapacitors based on the synergetic effect between aqueous Al^{3+} and ordered hexagonal tungsten oxide nanorod arrays. J. Mater. Chem. A *8*, 9927–9938. https://doi.org/10.1039/d0ta01808b.

57. Liu, Y., Sun, L., Sikha, G., Isidorsson, J., Lim, S., Anders, A., Leo Kwak, B., and Gordon, J.G. (2014). 2-D mathematical modeling for a large

electrochromic window–part I. Sol. Energy Mater. Sol. Cells *120*, 1–8. https://doi.org/10.1016/j.solmat.2013.07.030.

58. Li, J., Zhang, H., Cui, Y., Da, H., Cai, Y., and Zhang, S. (2022). Ultra-stable high voltage lithium metal batteries enabled by solid garnet electrolyte surface-engineered with a grafted aromatics layer. Chem. Eng. J. *450*, 138457. https://doi.org/10.1016/j.cej.2022.138457.
59. Zhang, J., Li, S., Wang, X., Mao, S., Guo, J., Shen, Z., Mao, J., Wu, Q., Shen, K., Cheng, H., et al. (2024). Construction of stable Li_2O-Rich solid electrolyte interphase for practical PEO-based Li-metal batteries. Adv. Energy Mater. *14*, 2302587. https://doi.org/10.1002/aenm.202302587.
60. Zhang, T., Kong, J., Shen, C., Cui, S., Lin, Z., Deng, Y., Song, M., Jiao, L., Huang, H., Jin, T., and Xie, K. (2023). Converting residual alkali into sodium compensation additive for high-energy Na-ion batteries. ACS Energy Lett. *8*, 4753–4761. https://doi.org/10.1021/acsenergylett.3c02075.